https://doi.org/10.1016/j.mtla.2019.100255

Phase-Field Modeling of Oxide Scale Roughening induced by outward growing oxide

Chen Lin, Haihui Ruan*

Department of Mechanical Engineering, The Hong Kong Polytechnic University

Hung Hom, Kowloon, Hong Kong, China

Abstract

A phase-field modeling of oxide roughening induced by outward growing oxide is proposed, which involves a reaction rate formula derived based on the detailed balance of a chemical system. The Allen-Cahn equation, in cooperation with the reaction-diffusion and mechanical equilibrium equations, are then established for describing the phase transformation, oxidation kinetics, elemental diffusion and mechanical deformation. The numerical simulations reveal that the oxide roughness is not only affected by chemical and mechanical properties but also the geometric features. By changing the initial surface morphology, the oxide roughness is significantly reduced, which would be a very effective and simple method in related industrial application.

Keyword: *Oxide scale roughening, phase-field model, Oxidation kinetics, Eigenstrain.*

* Corresponding author Tel.: + 852 2766 6648, Fax: +852 2365 4703, E-mail address: haihui.ruan@polyu.edu.hk

Nomenclature

$\mathbf{c}$	Concentration vector
$\mathbf{d}$	Displacement vector
$\boldsymbol{\varepsilon}$	Total strain
$\boldsymbol{\varepsilon}^{g}$	Eigenstrain
$\mathbf{D}^{e}$	Elastic stiffness matrix
$\boldsymbol{\sigma}$	Stress tensor
$\mathbf{I}$	Second-order identity tensor
μ	Chemical potential
ϕ	Phase index
λ	Scale factor of the interfacial energy density
σ	Interfacial energy density
ζ	Interfacial thickness
γ	Strength of interfacial anisotropy
PBR	Pilling-Bedworth ratio
r	Reaction rate
Λ	Dimensionless reaction driving force
L_{σ}	Coefficient of the contribution of interfacial energy
L_{κ}	Coefficient of the contribution of reaction kinetics
D	Diffusion coefficient

div	Divergence operator
∇	Gradient operator
∂	Partial differential symbol
δ	Variational symbol

Introduction

Evolutions of morphology of surface (or interface) play an important role in materials performance due to the significant effects on physical, chemical, and mechanical properties. Oxide formation, being one of the typical evolutions of surface morphology, has long been a research focus. The oxide scale, formed on the surfaces of alloys, protects the alloy components, such as the combustion chambers and the blades of gas turbine and aero-engine, from further degradation in the extremely high-temperature and oxidative environment [1]. The uncontrolled morphologies of surface (or interface) of oxide scale may also lead to irreversible failure. For instance, the non-uniform growth of oxide scale in thermal barrier coating (TBC) has been identified to be a detrimental factor to the TBC lifetime [2]. It would result in stress accumulation near oxide/substrate interface, which accelerates the damage development and leads to the premature spalling failure of TBC. Therefore, understanding surface morphology evolution mechanism of oxide scale would help in predicting the failure of materials or structures in complex service environment, and improve the material or structural design.

Many theoretical, numerical, and experimental approaches have been implemented to study the oxide growth and probe the oxidation mechanism [3-22]. The existing

phenomenological model describes a parabolic relation between time and average thickness of oxide layer, with the parameters determined through a long-term experiment (usually several hundred hours). This kind of phenomenological model, however, cannot capture the oxidation mechanism. The numerical model based on the classical Fick's first law could better predict the growth of an oxide. For example, the numerical studies conducted by Busso *et al*. [3] and Zhao *et al.* [4] demonstrated that the evolution of oxide scale was dependent on the concentration of reactants. Taking the consumption of reactants into account, Lin *et al*. [5, 6] proposed a diffusion-reaction model, in which the Fick's law was modified by adding an oxidation term.

The effect of mechanical loading on oxidation has also been experimentally demonstrated by Calvarin-Amiri *et al*. [7]. To study the stress-oxidation interaction, Krishnamurthy *et al.* [8] formulated an one dimensional (1D) model, in which the chemical potential was expressed in the form of hydrostatic stress dependent by following Larché and Cahn *et al.* [9] and the effect of stress on diffusion and inward oxide growth rate were considered. Following Krishnamurthy *et al.*'s approach. Zhou *et al.* [10] and Wang *et al.* [11] developed the more complicated 1D models. In Zhou's model [10], the chemical potential was dependent on both the hydrostatic and deviatoric stresses based on the formulae derived by Swaminathan *et al.* [12]. In Wang's model [11], the inelastic deformation was considered. However, their approaches are difficult to be extended to be beyond the 1D scenario. Based on a thermodynamically consistent framework, a 2D chemical-mechanical coupled model was proposed by Loeffel and Anand *et al.* [13, 14], in which the effect of mechanical

deformation energy on inward oxidation rate was considered and the influence of stress on diffusion was ignored. Anand's model [13, 14] has been further developed by Lin *et al*. [15], in which the hydrostatic stress dependent chemical potential [9] was employed and the effect of stress on diffusion was considered. The formulations of oxidation rate, however, might be unreasonable in Anand's and Lin's models, which lead to an unrealistic result that the oxidation rate is unaffected by mechanical deformation (see Fig. 15(a) in [14] and Fig 11 in [15]).

The growth of an oxide scale is affected not only by diffusion and mechanical deformation but also by other factors including oxidation kinetics, surface (or interface) energy, phase transformation and the morphology of the oxide scale. These factors are generally coupled, bringing about the complexity in a theoretical treatment. The phase-field model (PFM), rapidly developed in the last two decades, is an effective method to deal with problems with many coupled factors. PFM employs the diffusive interface to deal with morphology change without any priori assumptions on the shape of interface or any interface-tracking algorithms. By coupling the effects of thermal conduction, elemental diffusion, mechanical deformation and electric potential, PFM has been extended and utilized across many fields of materials science. A few applications of phase-field approach in the oxidation have been proposed. By using the principles of thermodynamics of irreversible processes, Ammar *et al*. [16] proposed a finite-element formulation of PFM to describe oxidation, in which the migration of phase interface was completely driven by the elemental diffusion. Zaeem *et al*. [17] presented a PFM to study the oxidation of pure metals, in which

the effect of elastic deformation induced by interface mismatch was considered. Fang *et al.* [18] further developed Zaeem's model to involve plastic deformation and creep. However, the limitation in these PFMs is that the kinetics of chemical reaction is still not considered.

Recently, Feng' group experimentally studied the morphology evolution of oxide surface during high temperature oxidation [19-22]. The surface roughening process of an originally flat oxide scale has been observed by in situ full-field measurement using the high temperature scanning probe microscopy (SPM). They heated an Ni specimen with a well-polished surface and obtained the change of surface morphology with time [22]. Their main results are recapped in Fig. 1, which shows the increase of roughness with oxidation time. It is noted that the growth rate of oxide humps is highly nonuniform and that the maximum growth rate about 7.6 nm/min within the initial 10 min oxidation at $700^{\circ}C$ (see Fig. 1(b)). These results cannot be explained based on the existing numerical models, which poses the need of a more elaborated model of oxidation.

Fig.1

In the present paper, we propose a PFM to investigate the evolution of surface morphology induced by oxidation. A formulation of oxidation rate, which is expressed in the form of chemical potentials of reactants and products and conforms to the detailed balance of reaction, is derived. The Gibbs free energy is established, in which contributions of chemical potential, mechanical deformation and interface are considered. Thus, the chemical potentials of reactants and products, which are the variational derivatives of the total free energy with respect to the corresponding concentration, can be derived. Noting that the formation of oxide

phase is only owing to the oxidation, the rate of oxidation and the rate of oxide phase transformation is equalized. Consequently, the general Allen-Cahn type equation is established to govern the evolution of oxide phase, which is convenient to capture the oxidation kinetics and the variations of elemental concentration and elastic energy. The model also formulates elemental diffusion and consumption as well as mechanical deformation and is applied to study formation of oxide on the pure metal Ni. With the model, we demonstrate that an originally flat oxide scale becomes increasingly roughened with time, which is in line with the experimental results of Li *et al.* [22] (See Fig. 1).

Methodology

For a numerical treatment of the growth of oxide (M_aO_b) on the pure metal substrate (M), we assume[1] that an infinitesimally thin oxide scale (M_aO_b) with perfect lattice structure has been on the metal substrate (M) and focus on the subsequent evolution of morphology of the growing oxide layer.

Fig. 2

Figure 2 illustrates schematically the oxidation process, which starts with a surface adsorption step. The gaseous oxygen (O_2) changes to the atomic oxygen (O) ($O_2 \rightarrow 2O$), which is then adsorbed onto the surface of the oxide scale [23]. If the adsorption is fast, the rate of the surface reaction is determined by the rate of the reaction with M in the oxide. The adsorbed oxygen atoms are then ionized by capturing the free electrons in the oxide layer, i.e. $O + 2e^- \rightarrow O^{2-}$, meanwhile the easily oxidized free metal (M) atoms in the substrate are converted to ions

[1] The onset stage of oxide formation is very complicated and is still lack of mechanism understanding [23, 24].

at the M_aO_b/M interface, i.e. $M \rightarrow M^{n+} + ne^-$ [24]. Consequently, counter diffusion leads to both the oxygen anion O^{2-} and metal cation M^{n+} diffuse into the oxide scale and then the oxidation takes place, i.e. $aM^{n+}+bO^{2-} \rightarrow M_aO_b$. Since the surface adsorption and ionizations are much faster than the oxidation, we do not consider the details of the adsorption and sub-reactions $O + 2e^- \rightarrow O^{2-}$, $M \rightarrow M^{n+} + ne^-$ and $aM^{n+}+bO^{2-} \rightarrow M_aO_b$ but formulate the schematic equation of oxidation reaction [8] as:

$$aM + bO \rightarrow M_aO_b . \tag{1}$$

Due to the difference in the diffusion rates of reactants, newly formed oxide might grow on the M_aO_b/M interface, called inward growing oxide, or on the M_aO_b/O interface, called outward growing oxide. In a metal (M)–oxide (M_aO_b)–gas (O) three phases system, the inward and outward growing oxide can be regarded as the metal (M) → oxide (M_aO_b) and gas (O) → oxide (M_aO_b) phase transformations, respectively. In this paper, we focus on the mechanism of surface roughening of NiO as reported by Feng *et al.* [22]. Many experiments [22, 25-27] have demonstrated that the NiO growing is dominated by the outward diffusion of Ni rather than the inward diffusion of oxygen. Therefore, the surface roughening of NiO should be attributed to the outward growing rather than the inward growing of the oxide scale. And a binary phase-field model, describing the gas (O) → oxide (M_aO_b) phase transformation, can be adopted.

Due to the lattice mismatch between oxide (M_aO_b) and metal substrate (M), considerable eigenstrains are resulted during oxidation. Owing to the constraint of metal substrate (M), these eigenstrains give rise to a significant in-plane compressive stress, as indicated in Fig. 2. The

contribution of mechanical energy induced by lattice mismatch must be included in the free energy of the system, so that the influence of mechanical deformation on the oxidation kinetics and phase transformation can be captured in governing equations.

2.1. Gibbs free energy

Considering the set of elemental concentrations, **c**, participating in the oxidation, and the displacement field, **d**, induced by the mismatch of lattice parameters between the oxide (M_aO_b) and the metal substrate (M), the Gibbs free energy of the system can be expressed as:

$$F = \int_{\Omega} \left[f_{\text{chem}}(\mathbf{c}) + f_{\text{grad}}(\mathbf{c}) + f_{\text{mech}}(\mathbf{c},\mathbf{d}) \right] dV , \tag{2}$$

where F is the total Gibbs free energy of a closed system, Ω; f_{chem}, f_{grad}, and f_{mech} are the chemical potential, gradient, and mechanical energy densities, respectively. Herein the set of elemental concentrations can be expressed as **c** = (c^{ox}, c^{O}, c^{met}), in which the superscripts $^{\text{ox}}$, $^{\text{O}}$, and $^{\text{met}}$ pertain to the oxide (M_aO_b), atomic oxygen (O) and metal (M). The concentration of electrons (e^-) is ignored in our formula since it contributes very weekly to the free energy when the electric field is absent. However, in studying an electrochemical process, say in battery or fuel cell, the concentration of electrons (e^-) should be involved. The concentrations can be further expressed in the dimensionless form, $\bar{c} = c/c_{\text{ref}}$, where the subscript $_{\text{ref}}$ indicates the maximum concentration.

Ignoring the interaction of multiple species, the chemical potential energy density can be expressed as:

$$f_{\text{chem}}(\mathbf{c}) = f_{\text{chem}}^{\text{met}}\left(c^{\text{met}}\right) + f_{\text{chem}}^{\text{O}}\left(c^{\text{O}}\right) + f_{\text{chem}}^{\text{ox}}\left(c^{\text{ox}}\right), \tag{3.a}$$

$$f_{\text{chem}}^{\text{met(or O)}} = c^{\text{met(or O)}} RT\left(\ln\left(\bar{c}^{\text{met(or O)}}\right) - 1\right) + c^{\text{met(or O)}} \mu_0^{\text{met(or O)}}, \tag{3.b}$$

$$f_{\text{chem}}^{\text{ox}} = Wg\left(\bar{c}^{\text{ox}}\right) = W\left(\bar{c}^{\text{ox}}\right)^2\left(\bar{c}^{\text{ox}} - 1\right)^2, \tag{3.c}$$

where $f_{\text{chem}}^{\text{met(or O)}}$ is the chemical potential energy density owing to the existence of reactants (free metal or oxygen atoms) in the oxide lattice, which is established following Loeffel and Anand *et al.* [13], $f_{\text{chem}}^{\text{ox}}$ is a double-well function to describe the energy barrier between gas and oxide phases, which is zero in both oxide and gas phases but varies continuously in the diffusive interface of a finite width. In Eqs. (3.b), R is the ideal gas constant, T is the thermodynamic temperature, μ_0 is the chemical potential. In Eq. (3.c), W is the height of the energy barrier and is related to the interfacial energy (per unit area), σ, and the interfacial thickness, ζ, in the form of $W = 18\sigma/\zeta$ [16]. The phase index, ϕ, corresponding to the dimensionless concentration of oxide (M_aO_b), is given as:

$$\phi = \bar{c}^{\text{ox}}. \tag{4}$$

In this case, the chemical potential energy density can be recast as:

$$f_{\text{chem}} = \left[c^{\text{met}}RT\left(\ln\left(\bar{c}^{\text{met}}\right) - 1\right) + c^{\text{met}}\mu_0^{\text{met}}\right] + \left[c^{\text{O}}RT\left(\ln\left(\bar{c}^{\text{O}}\right) - 1\right) + c^{\text{O}}\mu_0^{\text{O}}\right] + Wg\left(\phi\right). \tag{5}$$

With the diffusive interface, the gradient energy density, f_{grad} (**c**), can also be expressed in terms of the phase index, ϕ, as:

$$f_{\text{grad}}\left(\mathbf{c}\right) = f_{\text{grad}}\left(\phi\right) = \frac{\lambda^2}{2}\left|\nabla\phi\right|^2, \tag{6}$$

where ∇ is the gradient operator, and λ is the scale factor of the interfacial energy density. If the interface is isotropic with energy density (per unit area), σ, and interfacial thickness, ζ, it is known that $\lambda^2 = \sigma\zeta$ [16]. The interface is usually considered to be anisotropic owing to the orientation of oxide lattice. The anisotropic interfacial energy and thickness are expressed as σ

= $\sigma_0\eta(\theta)$ and $\zeta = \zeta_0\eta(\theta)$, respectively, where $\eta(\theta)$ is the anisotropic function [28] and θ is the normal direction of interface, expressed as:

$$\eta(\theta)=\begin{cases}\dfrac{1+\gamma\cos(2\theta_m)}{\cos(\theta_m)}\cos(\theta-\theta_0) & -\theta_m<\theta-\theta_0<\theta_m\\ -\dfrac{1+\gamma\cos(2\theta_m)}{\cos(\theta_m)}\cos(\theta-\theta_0) & -\pi-\theta_m<\theta-\theta_0<-\pi+\theta_m\\ -\dfrac{1+\gamma\cos(2\theta_m)}{\cos(\theta_m)}\cos(\theta-\theta_0) & \pi-\theta_m<\theta-\theta_0<\pi+\theta_m\\ 1+\gamma\cos\left(2(\theta-\theta_0)\right) & \text{ohter}\end{cases}, \tag{7}$$

where γ is the strength of interfacial anisotropy, θ_0 represents the fastest growth direction, θ_m is constant which can be determined by solving the equation $\eta(\theta_m+\theta_0)\sin(\theta_m)+\eta'(\theta_m+\theta_0)\cos(\theta_m)=0$, where $\eta'(\theta) = d\eta(\theta)/d\theta$. For more clarity, the evolution of anisotropic function, $\eta(\theta)$, with the intersection angle between normal direction of interface and the fastest growth direction, θ - θ_0 , and the strength of interfacial anisotropy, γ, are illustrated in Fig. 3.

Fig. 3

For phase filed model, the mechanical energy density is defined as:

$$f_{\text{mech}}(\mathbf{c},\mathbf{d}) = f_{\text{mech}}(\phi,\mathbf{d}) = \frac{1}{2}\left(\left(\boldsymbol{\varepsilon}^{\text{e}}(\phi,\mathbf{d})\right)^{T}\cdot\left(\mathbf{D}^{\text{e}}(\phi)\boldsymbol{\varepsilon}^{\text{e}}(\phi,\mathbf{d})\right)\right), \tag{8}$$

where $\mathbf{D}^{\text{e}}$ and $\boldsymbol{\varepsilon}^{\text{e}}$ are the stiffness matrix and the elastic strain tensor, respectively. To allow for a continuous description across the oxide-gas interface, they are expressed as [29]:

$$\mathbf{D}^{\text{e}} = p(\phi)\mathbf{D}^{\text{e}}_{\text{ox}}, \tag{9.a}$$

$$\boldsymbol{\varepsilon}^{\text{e}} = \boldsymbol{\varepsilon} - p(\phi)\boldsymbol{\varepsilon}^{\text{g}}, \tag{9.b}$$

where $\mathbf{D}^{\text{e}}_{\text{ox}}$ is the stiffness matrix of oxide phase, $\boldsymbol{\varepsilon}$ is the total strain and $\boldsymbol{\varepsilon}^{\text{g}}$ is the anisotropic

eigenstrain tensor, describing the lattice mismatch between oxide and substrate, which can be obtained by the Pilling-Bedworth ratio (*PBR*) (See Appendix A). $p(\phi)$ is the interpolation function to mollify the discontinuity. It satisfies the conditions that $p(0)=0$ and $p(1)=1$ and that $p(\phi)$ is extremum at $\phi=0$ and $\phi=1$. Following Wang *et al.* [30], the appropriate choice of $p(\phi)$ can be given in the form: $p(\phi)=\phi^3\left(10-15\phi+6\phi^2\right)$. Substituting Eqs. (9.a, 9.b) into Eq. (8) leads to the mechanical energy density:

$$f_{\text{mech}}(\phi,\mathbf{d})=p(\phi)\frac{1}{2}\left(\left(\boldsymbol{\varepsilon}-p(\phi)\boldsymbol{\varepsilon}^{\text{g}}\right)^{T}\cdot\left(\mathbf{D}_{\text{ox}}^{\text{e}}\left(\boldsymbol{\varepsilon}-p(\phi)\boldsymbol{\varepsilon}^{\text{g}}\right)\right)\right), \tag{10}$$

The total strain, $\boldsymbol{\varepsilon}$, is derived from geometric relation under the assumption of small deformation:

$$\boldsymbol{\varepsilon}=\left\{\varepsilon_{ij}\right\}=\left\{\frac{1}{2}\left(\frac{\partial d_i}{\partial x_j}+\frac{\partial d_j}{\partial x_i}\right)\right\}\ \left(i=1,2,3;\ j=1,2,3\right), \tag{11}$$

where ∂ is the partial differential symbol. The stress tensor is then given as $\boldsymbol{\sigma}=\mathbf{D}^{\text{e}}\boldsymbol{\varepsilon}^{\text{e}}$, which satisfies the equilibrium equation:

$$\text{div}\left(\boldsymbol{\sigma}\right)=0, \tag{12}$$

where div is the divergence operator and body force is neglected. Substituting Eqs. (9.a, 9.b and 11) into Eq. (12) leads to the governing equation of displacement field $\mathbf{d}$:

$$\text{div}\left[\left(p(\phi)\mathbf{D}^{\text{e}}\right)\left(\left\{\frac{1}{2}\left(\frac{\partial d_i}{\partial x_j}+\frac{\partial d_j}{\partial x_i}\right)\right\}-p(\phi)\boldsymbol{\varepsilon}^{\text{g}}\right)\right]=0, \tag{13}$$

Base on Eq. (13), the mechanical deformation induced by oxidation can be calculated.

2.2. Evolution equation

During oxidation, the forward and backward reactions take place simultaneously. If the forward reaction is more favorable, there would be a net increase of the product (M_aO_b). To

describe the oxidation kinetics, the forward and backward reaction rates, satisfying the detailed balance of the chemical system [31], are given as:

$$r_{1\to 2}=k_0 e^{-(\mu_{TS}-\mu_1)/RT}, \tag{14.a}$$

$$r_{2\to 1}=k_0 e^{-(\mu_{TS}-\mu_2)/RT}, \tag{14.b}$$

And the net reaction rate is:

$$r_{net}=r_{1\to 2}-r_{2\to 1}=k_0\left(e^{-(\mu_{TS}-\mu_1)/RT}-e^{-(\mu_{TS}-\mu_2)/RT}\right), \tag{14.c}$$

where $r_{1\to 2}$, $r_{2\to 1}$ and r_{net} represent the forward, backward and net oxidation rate, respectively, μ_1 and μ_2 are the chemical potential of reactants and products, respectively, μ_{TS} is the chemical potential at the transition state, k_0 is the coefficient of oxidation rate. The chemical potential of reactants, μ_1, and products, μ_2, can further be expressed as:

$$\mu_1 = a\mu^{met}+b\mu^{O}, \tag{15.a}$$

$$\text{and}\quad \mu_2=\mu^{ox}, \tag{15.b}$$

where μ^{met}, μ^{O} and μ^{ox} are the chemical potential of atomic metal (M), atomic oxygen (O) and oxide (M_aO_b), respectively. They are the variational derivatives of the total free energy, F, with respect to the corresponding concentration [32], given as:

$$\mu^{met\ (or\ O)}=\frac{\delta F}{\delta c^{met\ (or\ O)}}=RT\ln\left(\bar{c}^{met\ (or\ O)}\right)+\mu_0^{met\ (or\ O)}, \tag{16.a}$$

and

$$\mu^{ox}=\frac{\delta F}{\delta c^{ox}}=\frac{1}{c_{ref}^{ox}}\left(W\frac{\partial g(\phi)}{\partial\phi}-\sigma^0\zeta^0\left(\eta^2\nabla^2\phi-\frac{\partial}{\partial x}\left(\eta\eta'\frac{\partial\phi}{\partial y}\right)+\frac{\partial}{\partial y}\left(\eta\eta'\frac{\partial\phi}{\partial x}\right)\right)\right)+\frac{\partial f_{mech}}{c_{ref}^{ox}\partial\phi}. \tag{16.b}$$

where δ is the variational symbol. Substituting Eq. (16.a) into Eq. (15.a), the chemical potential of reactants can be given as:

$$\begin{aligned}\mu_1 &= RT\ln\left[\left(\bar{c}^{\,\mathrm{met}}\right)^a\left(\bar{c}^{\,\mathrm{O}}\right)^b\right]+\left(a\mu_0^{\mathrm{met}}+b\mu_0^{\mathrm{O}}\right),\\ &= \mu_1^{\mathrm{diff}}+\mu_1^{\mathrm{ex}}\end{aligned} \tag{17}$$

where $\mu_1^{\mathrm{diff}} = RT\ln\left[\left(\bar{c}^{\,\mathrm{met}}\right)^a\left(\bar{c}^{\,\mathrm{O}}\right)^b\right]$ is the chemical potential that drives diffusion, and $\mu_1^{\mathrm{ex}} = a\mu_0^{\mathrm{met}}+b\mu_0^{\mathrm{O}}$ is the excess chemical potential that originates from the contributions of mechanical deformation and electrostatic field. The corresponding chemical potential of products can also be expressed in the form of $\mu_2 = \mu_2^{\mathrm{diff}}+\mu_2^{\mathrm{ex}}$, where μ_2^{diff} and μ_2^{ex} are, respectively, expressed as:

$$\mu_2^{\mathrm{diff}} = \frac{1}{c_{\mathrm{ref}}^{\mathrm{ox}}}\left(W\frac{\partial g(\phi)}{\partial\phi}-\sigma^0\zeta^0\left(\eta^2\nabla^2\phi-\frac{\partial}{\partial x}\left(\eta\eta'\frac{\partial\phi}{\partial y}\right)+\frac{\partial}{\partial y}\left(\eta\eta'\frac{\partial\phi}{\partial x}\right)\right)\right), \tag{18.a}$$

and

$$\mu_2^{\mathrm{ex}} = \frac{\partial f_{\mathrm{mech}}}{c_{\mathrm{ref}}^{\mathrm{ox}}\partial\phi} = \frac{1}{c_{\mathrm{ref}}^{\mathrm{ox}}}\left\{\begin{array}{l}\frac{1}{2}\left(\frac{\partial p(\phi)}{\partial\phi}\left(\boldsymbol{\varepsilon}-p(\phi)\boldsymbol{\varepsilon}^{\mathrm{g}}\right)^T\cdot\left(\mathbf{D}_{\mathrm{ox}}^{\mathrm{e}}\left(\boldsymbol{\varepsilon}-p(\phi)\boldsymbol{\varepsilon}^{\mathrm{g}}\right)\right)\right)+\\ \left(p(\phi)\left(\boldsymbol{\varepsilon}-p(\phi)\boldsymbol{\varepsilon}^{\mathrm{g}}\right)^T\cdot\left(\mathbf{D}_{\mathrm{ox}}^{\mathrm{e}}\left(\frac{\partial\boldsymbol{\varepsilon}}{\partial\phi}-\frac{\partial p(\phi)}{\partial\phi}\boldsymbol{\varepsilon}^{\mathrm{g}}\right)\right)\right)\end{array}\right\}. \tag{18.b}$$

The chemical potential at the transition state, μ_{TS}, is defined as:

$$\begin{aligned}\mu_{\mathrm{TS}} &= \mu_{\mathrm{TS}}^{\mathrm{diff}}+\mu_{\mathrm{TS}}^{\mathrm{ex}}\\ &= \mu_{\mathrm{TS}}^{\mathrm{diff}}+\left(\rho\mu_1^{\mathrm{ex}}+(1-\rho)\mu_2^{\mathrm{ex}}\right),\end{aligned} \tag{19}$$

where the excess chemical potential for transition state, $\mu_{\mathrm{TS}}^{\mathrm{ex}}$, is the linear combination of excess chemical potentials of the reactants and products with the asymmetry factor ρ ($1 > \rho > 0$) [30, 32].

Substituting Eqs. (18.a), (18.b) and (19) into Eq. (14.c), the oxidation rate can be expressed as:

$$r_{\mathrm{net}} = \frac{k_0}{\exp\left(\mu_{\mathrm{TS}}^{\mathrm{diff}}/RT\right)}\left(\exp\left(\frac{\mu_1^{\mathrm{diff}}-\rho\left(\mu_2^{\mathrm{ex}}-\mu_1^{\mathrm{ex}}\right)}{RT}\right)-\exp\left(\frac{\mu_2^{\mathrm{diff}}+(1-\rho)\left(\mu_2^{\mathrm{ex}}-\mu_1^{\mathrm{ex}}\right)}{RT}\right)\right). \tag{20}$$

Noting that the contribution of interfacial energy to oxidation is much smaller than the chemical and mechanical contribution, the oxidation rate can also be approximately rewritten as:

$$r_{\text{net}}=\frac{k_0}{\exp\left(\mu_{\text{TS}}^{\text{diff}}/RT\right)}\left(\exp\left(\frac{\mu_1^{\text{diff}}-\rho\left(\mu_2^{\text{ex}}-\mu_1^{\text{ex}}\right)}{RT}\right)-\left(1+\frac{\mu_2^{\text{diff}}}{RT}\right)\exp\left(\frac{(1-\rho)\left(\mu_2^{\text{ex}}-\mu_1^{\text{ex}}\right)}{RT}\right)\right). \quad (21)$$

It is apparent that the growth of oxide phase is only due to the oxidation. Thus, the relation between oxidation rate and oxide phase formation rate is given as $\partial\phi/\partial t=r_{\text{net}}$ [33]. By incorporating the expressions of μ_2^{diff} and μ_2^{ex}, the rate of oxide phase formation can be expressed as:

$$\frac{\partial\phi}{\partial t}=-L_\sigma\left(W\frac{\partial g(\phi)}{\partial\phi}-\sigma^0\zeta^0\left(\eta^2\nabla^2\phi-\frac{\partial}{\partial x}\left(\eta\eta'\frac{\partial\phi}{\partial y}\right)+\frac{\partial}{\partial y}\left(\eta\eta'\frac{\partial\phi}{\partial x}\right)\right)\right)- L_\kappa\left(e^{-(1-\rho)\Lambda}-\left(\bar{c}^{\text{met}}\right)^a\left(\bar{c}^{\text{O}}\right)^b e^{\rho\Lambda}\right), \quad (22)$$

where L_σ and L_κ are coefficients to scale the contributions of the interfacial energy and the oxidation kinetics to the phase migration, respectively, and Λ is defined as the dimensionless reaction driving force. They are respectively expressed as:

$$L_\sigma=\frac{k_0}{c_{\text{ref}}^{\text{ox}}RT\exp\left(\mu_{\text{TS}}^{\text{diff}}/RT\right)}\exp\left(\frac{(1-\rho)\left(\mu_2^{\text{ex}}-\mu_1^{\text{ex}}\right)}{RT}\right), \quad (23.a)$$

$$L_\kappa=\frac{k_0}{\exp\left(\mu_{\text{TS}}^{\text{diff}}/RT\right)}, \quad (23.b)$$

and

$$\Lambda=\frac{\mu_1^{\text{ex}}-\left(\partial f_{\text{mech}}/\partial\phi\right)/c_{\text{ref}}^{\text{ox}}}{RT}. \quad (23.c)$$

In the present model, L_σ and L_κ are assumed to be constant for simplicity. As expressed in

Eq. (22), the contribution to phase transformation is divided into two parts: one is the interfacial energy (the first term in the right-hand side); and the other is the oxidation kinetics (the second term in the right-hand side). The interfacial energy is spatially continuous, while the oxidation kinetics is spatially discontinuous, which is still not implementable in a numerical scheme. Considering the fact that the oxidation only occurs at the interface, the spatially continuous function, $\partial p(\phi)/\partial\phi$, is used to mollify the discontinuity, which is zero at $\phi=1$ (oxide phase) and $\phi=0$ (gas phase) and is symmetric about $\phi=0.5$. Consequently, the rate of phase transformation can be expressed as follows:

$$\frac{\partial\phi}{\partial t}=-L_\sigma\left(W\frac{\partial g(\phi)}{\partial\phi}-\sigma^0\zeta^0\left(\eta^2\nabla^2\phi-\frac{\partial}{\partial x}\left(\eta\eta'\frac{\partial\phi}{\partial y}\right)+\frac{\partial}{\partial y}\left(\eta\eta'\frac{\partial\phi}{\partial x}\right)\right)\right)- L_\kappa\frac{\partial p(\phi)}{\partial\phi}\left(e^{-(1-\rho)\Lambda}-\left(\bar{c}^{\,\mathrm{met}}\right)^a\left(\bar{c}^{\,\mathrm{O}}\right)^b e^{\rho\Lambda}\right) \quad (24)$$

It is obvious that Eq. (24) is consistent with the general Allen-Cahn type equation of the phase index, ϕ, in PFM, which includes the additional contribution of oxidation kinetics.

The evolution of concentration of reactants, considering reaction and diffusion, can be given as:

$$\frac{\partial c^{\mathrm{met\ (or\ O)}}}{\partial t}=\nabla\left(D^{\mathrm{met\ (or\ O)}}\nabla c^{\mathrm{met\ (or\ O)}}\right)-a\left(\mathrm{or}\ b\right)c_{\mathrm{ref}}^{\mathrm{ox}}\frac{\partial\phi}{\partial t}. \quad (25)$$

In Eq. (25), the first term on the right-hand side describe the elemental diffusion and the second term on the right-hand side represents the elemental consumption (per unit time and unit volume). Apparently, the elemental consumption is related to the production of oxide (M_aO_b), i.e., the generation of one mole oxide (M_aO_b) requires the consumption of *a* mole metal atoms and *b* mole oxygen atoms. *D* is the diffusion coefficient, expressed as

$D^{\text{met(or O)}} = \left(D_{\text{ox}}^{\text{met (or O)}}\right)^{p(\phi)} \left(D_{\text{gas}}^{\text{met (or O)}}\right)^{1-p(\phi)}$ with $D_{\text{ox}}^{\text{met (or O)}}$ and $D_{\text{gas}}^{\text{met (or O)}}$ being the diffusion coefficients of metal (M) or oxygen (O) in the oxide and gas phase, respectively. Considering the effect of grain boundaries, the diffusion coefficients of metal (M) or oxygen (O) in the oxide can be further expressed in the form of [26]:

$$D_{\text{ox}} = \left(2\, w_{\text{gb}} / d_{\text{g}}\right) D_{\text{gb}} + \left(1 - 2\, w_{\text{gb}} / d_{\text{g}}\right) D_{\text{g}}, \tag{26}$$

where D_{gb} and D_{g} represent the diffusion coefficients in grain boundary and grain, respectively, w_{gb} and d_{g} are the width of grain boundary and the grain diameter of oxide.

By defining the reference length l_{ref}, reference time t_{ref}, and reference energy density f_{ref}, the non-dimensional evolution equations can be derived for numerical simulation. (See Appendix B)

Numerical analysis

3.1. One-dimension oxidation simulation

Before the study of surface roughening, one-dimension (1D) numerical simulation is implemented for validating the proposed phase-field model and giving a preliminary understanding of the oxidation behavior. To have an analytical solution, the effect of elemental diffusion and mechanical deformation is ignored and the governing equations (Eqs. (13), (24) and (25)) can be reduced to:

$$\frac{\partial \phi}{\partial t} = -L_{\sigma}\left(W \frac{\partial g(\phi)}{\partial \phi} - \sigma^{0}\zeta^{0} \frac{\partial^{2}\phi}{\partial x^{2}}\right) - L_{\kappa} \frac{\partial p(\phi)}{\partial \phi}\left(e^{-(1-\rho)\Lambda} - \left(\bar{c}^{\text{met}}\right)^{a}\left(\bar{c}^{\text{O}}\right)^{b} e^{\rho\Lambda}\right), \tag{27}$$

where $\bar{c}^{\text{met}}$ and $\bar{c}^{\text{O}}$ are set to be constants to remove the effect of elemental diffusion. The steady-state theoretical solution of Eq. (27) is in the form of a hyperbolic-tangent type [34], ϕ

= 0.5tanh(3(x-vt)/ζ^0) + 0.5, where v is the velocity of phase migration. The 1D analytical solution of v can be derived as:

$$v = L_\kappa \zeta^0 \left(\left(\bar{c}^{\,\mathrm{met}} \right)^a \left(\bar{c}^{\,\mathrm{O}} \right)^b e^{\rho\Lambda} - e^{-(1-\rho)\Lambda} \right). \tag{28}$$

Fig. 4

Setting $\bar{c}^{\,\mathrm{met}} = \bar{c}^{\,\mathrm{O}} = 1$, the velocity of phase migration, v, as the function of the dimensionless reaction driving force, Λ, and the asymmetry factor, ρ, can be numerically calculated and compared with the analytical result (Eq. (28)). Fig. 4(a) shows the consistence between analytical and numerical results, which validates the numerical code. If we set $\bar{c}^{\,\mathrm{O}} = 1$ and v = 0, the critical elemental concentration, $\bar{c}_{\mathrm{cr}}^{\mathrm{met}}$, can also be obtained from Eq. (28), which means that the oxidation could be restricted, if the local concentration of reactants is smaller than the critical value. The relation between critical elemental concentration, $\bar{c}_{\mathrm{cr}}^{\mathrm{met}}$, and the reaction driving force, Λ, was obtained by solving Eq. (28). Thus, the accuracy of the numerical code can be further verified by the comparison between simulation results and the analytical results from Eq. (28), which is shown Fig. 4(b).

A slow diffusion can bring about insufficient reactants, thus inhibits oxidation. In addition, the lattice mismatch between oxide (M_aO_b) and the metal substrate (M) leads to the considerable eigenstrain, which induces the mechanical energy in the oxide layer. It elevates the chemical potential of oxide and reduces the reaction driving force, Λ, as expressed in Eq. (23. c). With the increase of eigenstrain, the reaction rate reduces. When the eigenstrain is larger than a critical value, oxidation could also be stopped. In the above discussion, both diffusion and mechanical deformation are ignored. In order to study their effects, we should

consider more general cases.

Fig. 5

Let us take the oxidation of pure metal Ni at 928K as an example. The simulation model is a $200\ \text{nm} \times 300\ \text{nm}$ box for the oxide-gas binary-phase system, as shown in Fig. 5, where the initial thickness of oxide layer is set to be 20nm with the flat interface to model the 1D oxidation behavior. The zero-flux boundary conditions are applied to all sides for phase evolution. The initial displacements are set to zero in the whole domain. The top side is unconstrained, while the other sides are constraint along their normal direction. The initial dimensionless Ni concentration is set to be 1 in the oxide phase and 0 in the gas phase. For boundary conditions, the Ni concentration at the bottom is $\bar{c}^{\text{met}} = 1$ to ensure that the oxidation can continue; the dimensionless concentration of atomic oxygen, $\bar{c}^{\text{O}}$, at the oxide side of the oxide-gas interface is also set to be 1 since the adsorption is much faster than oxidation; and the zero-flux conditions are applied to other sides. Since many experiments [22, 25-27] have demonstrated that the growth of oxide (NiO) is dominated by the outward diffusion of Ni rather than the inward diffusion of oxygen, the only outward growing of oxide is simulated and no diffusion of oxygen in the oxide occurs and only the diffusion of Ni is assumed.

Table 1

The chemical potential of reactant, μ_1^{ex}, is set to be $2RT$, so that the maximum dimensionless reaction driving force, Λ, is 2. Judged from Fig. 1, the maximum growth rate of an oxide hump is about 76 nm within the initial 10 min at 928K (see Fig. 1(b)). Thus, in

simulation, the maximum interface migration velocity is set to be 8 nm/min. Based on the theoretical solution of interface migration velocity, the coefficient, L_κ, is obtained to be 0.075/min with the parameters ζ_0 = 10 nm, $\overline{c}^{\,\mathrm{met}} = \overline{c}^{\,\mathrm{O}} = 1$, a = b = 1 and ρ = 0.8. The oxidation is associated with volumetric expansion. For Ni, the average eigenstrain, obtained by *PBR*, is about 0.2 (See Appendix A). The eigenstrain, however, is not isotropic, i.e. the in-plane transverse strain, $\varepsilon_{11}^{\mathrm{g}}$, is usually smaller than the out-of-plane strain, $\varepsilon_{22}^{\mathrm{g}}$, for a 2D scenario. The ratio, $\varepsilon_{11}^{\mathrm{g}}/\varepsilon_{22}^{\mathrm{g}}$, could be as small as 1/87 from the results of Huntz *et al.* [36]. Evans *et al.* [37] indicate that the in-plane transverse strain, $\varepsilon_{11}^{\mathrm{g}}$, rather than the out-of-plane strain, $\varepsilon_{22}^{\mathrm{g}}$, is the main cause of the compressive stress and the elastic energy in the oxide layer. Thus, in the simulation, the out-of-plane strain, $\varepsilon_{22}^{\mathrm{g}}$, is set to be 0 and only the in-plane transverse strain, $\varepsilon_{11}^{\mathrm{g}}$, is considered, which is varied in the range of (0 ~ 0.1). The diffusion coefficient, $D_{\mathrm{ox}}^{\mathrm{met}}$, is calculated under the condition that the grain diameter, d_{g}, is 0.2 μm and the gas pressure is 1bar. A.M. Huntz *et al.* [25] have experimentally measured the grain diameter of the oxide NiO, which would vary with oxidation time from 0.2 μm to 1 μm, leading to the decreasing of diffusion coefficient, $D_{\mathrm{ox}}^{\mathrm{met}}$, from 1.85×10^{-16} to 3.7×10^{-17} $\mathrm{m^2/s}$. In addition, many experiments [25-27] have demonstrated that the magnitude of applied gas pressure also affects the diffusion coefficient, $D_{\mathrm{ox}}^{\mathrm{met}}$. Thus, in present simulation, the $D_{\mathrm{ox}}^{\mathrm{met}}$ also varies in the wider range of (1.85×10^{-17} ~ 1.85×10^{-15} $\mathrm{m^2/s}$). In simulation, the reference length, l_{ref}, and reference time, t_{ref}, are is 10 nm and 2 min, respectively. The commercial finite element package, COMSOL Multiphasic [38], is employed to solve governing equations. To guarantee the convergence of the solution, the calculation domain is discretized

by uniform square mesh with the size of 2 nm, i.e., $l_{\text{ref}}/5$ and the initial and maximum time step are both $t_{\text{ref}}/100$ for temporal integration.

Fig. 6

The increment of oxide layer thickness, Δh^{ox}, after 30-min oxidation against the variation of eigenstrain, $\varepsilon_{11}^{\text{g}}$, and diffusion coefficient, $D_{\text{ox}}^{\text{met}}$, is plotted in Fig. 6(a), where $D_{\text{ox, ref}}^{\text{met}} = 1.85\times10^{-16}\,\text{m}^2/\text{s}$ and $\varepsilon_{\text{ref}}^{\text{g}}$ = 0.055 are the reference diffusion coefficient and eigenstrain, respectively. It is observed that the thickness, Δh^{ox}, is approximately logarithmically dependent on the diffusion coefficient, $D_{\text{ox}}^{\text{met}}$, meaning that the slower diffusion leads to the more significant restraint on the growth of oxide layer. In contrast, the larger eigenstrain leads to the smaller Δh^{ox}. The relation between the thickness, Δh^{ox}, and the value $\left(\varepsilon_{11}^{g}\right)^2$ is approximately exponential as observed in Fig. 6(a), which is consistent with the exponential relation given in Eq. (27). The zero increment of thickness for oxide layer can be obtained, when the eigenstrain is as large as 0.055.

Since both the reduction of diffusion and the elevation of the eigenstrain could suppress the oxidation, a quantitative analysis is necessary to distinguish the major and secondary influencing factors. The contour of Fig, 5(a), in terms of relations between diffusion coefficient, $D_{\text{ox}}^{\text{met}}$, and eigenstrain, $\varepsilon_{11}^{\text{g}}$, for constant values of Δh^{ox}, is plotted in Fig. 6(b). It is noted that the curves relating $D_{\text{ox}}^{\text{met}}$ and $\varepsilon_{11}^{\text{g}}$ are quite flat, when $D_{\text{ox}}^{\text{met}}$ is small. The curves then gradually inflect and become almost vertical. It indicates that when $\varepsilon_{11}^{\text{g}}$ is large, the effect of elemental diffusion is suppressed. The curvature of the curves, which describes the inflection, can be used to quantitatively assess the relative importance of diffusion

coefficient, D_{ox}^{met}, and eigenstrain, ε_{11}^{g}. If the curvature is small, diffusion is important. The influence of diffusion then gradually fades out with the increase of ε_{11}^{g}. When the curvature is sufficient large, the diffusion rate has almost no effect on the growth speed of the oxide layer.

3.2. Two-dimension oxidation simulation (Oxide layer roughening)

3.2.1 Oxide layer roughening affected by chemical, mechanical, and interfacial properties

To study the surface roughening behavior during oxidation, the 2D phase-field model is implemented. The geometry and boundary conditions used in the simulation are shown in Fig. 5. The oxide-gas interface is assumed to be initially rough with a sinusoidal hump. Because of symmetry, only a half of the hump is used in the numerical simulation. The height of the sinusoidal hump is to represent the initial surface roughness, which is set to be Ra_{ini} = 30 nm based on the experimental measurement [22]. And the initial half width of the hump is also set to be b_{ini} = 30 nm. The diffusion coefficient and eigenstrain are varied from 1.85×10^{-17} to 1.85×10^{-15} m^2/s and from 0.004 to 0.055, respectively. The interfacial anisotropy is also considered, though there is no evidence to show that the oxide has strong orientation at the interphase boundary. The interfacial anisotropic parameter is chosen to be γ = 0.2, which is small comparing to other studies. For example, γ is usually chosen to be 0.3 ~ 0.6 in the study of the Widmanstätten Ferrite (WF) formation [28].

Fig. 7

The contour plots of the elastic energy, the concentration of Ni, and the reaction rate are shown in Fig. 7. It is observed that different magnitudes of diffusion coefficient and

eigenstrain lead to different surface patterns of the oxide layer. When the eigenstrain is 0.004 (Fig. 7(a ~ c)), the elemental diffusion is the main factor affecting the morphology evolution of the oxide layer. The homogeneous diffusion makes the initially rough surface become flatter. When the eigenstrain is 0.02 (Fig. 7(d ~ f)), the high elastic energy concentration can be observed around the flat part of the oxide scale which slows down the growth of the oxide layer. Since the convex part is much less deformed, the oxidation in the convex region is hardly affect by the eigenstrain. Thus, the inhomogeneous growth of oxide layer is observed in Fig. 7(d ~ f). In addition, the surface wrinkling, resembling those induced by surface instability, is observed. This is owing to the inhomogeneous distribution of elastic energy, which concentrates at the intersection of the flat and the humped surfaces, triggering the formation of a new hump adjacent to the original one. With the formation of humps, the redistribution of elastic energy leads to the more humps. Consequently, the corrugated surface is resulted. The further increase of the eigenstrain to 0.055 leads to the suppression of the oxide growth from the flat surface. The initial hump becomes bigger, leading to the dome-like surface morphology (Fig. 7(g ~ i)).

Fig. 8

While this eigenstrain plays the dominant role in forming the morphology of the oxide surface, the effect of diffusion coefficient cannot be completely ignored. In the map with the abscissa of ε_{11}^{g} and the ordinate of D_{ox}^{met}, the observed three different surface morphologies occurs at three different regions. We conducted simulations to identify the boundaries of the three regions and gives fitting equation for plotting the boundary curves, as shown in Fig. 8.

It is observed that the pattern of oxide layer is mainly affected by the eigenstrain and that the boundaries bend towards the smaller eigenstrain when the diffusion coefficient is small.

Fig. 9

As above mentioned, when the eigenstrain is large than 0.055, the oxidation could be completely suppressed at the flat region of the oxide surface while the hump grows larger, leading to the higher roughness. In case of ε_{11}^{g} = 0.055, the effects of elemental diffusion and the interfacial anisotropy are worthy of further study. To elaborate their effects, numerical studies using different diffusion coefficient, D_{ox}^{met}, and anisotropic parameter, γ, were carried out. We change D_{ox}^{met} and γ in the wide ranges of 1.85×10^{-17} ~ 1.85×10^{-15} m^2/s and 0 ~ 0.6, respectively. Fig. 9(a) shows the variation of the roughness of the oxide layer after 30-min oxidation against the change of D_{ox}^{met} and γ. It is observed that the roughness is almost linearly dependent on γ, when D_{ox}^{met} is large. While D_{ox}^{met} is small, the increase of roughness is also slowed down with the increase of γ, because the higher roughness of the oxide layer leads to the lower concentration of metal atoms at the vertices of asperities, leading to the reduction of the reaction rate. Fig. 9(b) is the 2D contour plot of Fig. 9(a), which can be used to study the relative effect of the two parameters based on the curvatures of contour curves.

The aspect ratio (height to width) of an asperity, Ψ, is another important measurable parameter to characterize the morphology of rough surface. Its variation with parameters γ and D_{ox}^{met} is plotted in Fig. 9(c). It is observed that the aspect ratio increases with the increase of γ or D_{ox}^{met}. The maximum aspect ratio, Ψ = 1.38, however, is much smaller than the measured aspect ratio for Widmanstätten Ferrite which is in the range of (10 ~ 100). This

is because that the growth of Widmanstätten Ferrite is mainly promoted by elemental diffusion which is inhomogeneous, i.e. the elemental diffusion is extremely faster at the tip of Widmanstätten Ferrite than that at the sides of Widmanstätten Ferrite [28]. The corresponding contour plot is shown in Fig. 9(d) to study the relative importance of $D_{\mathrm{ox}}^{\mathrm{met}}$ and γ.

3.2.2 Oxide layer roughening affected by initial geometric features

Fig. 10

The oxide roughening is affected not only by the chemical, mechanical, and interfacial properties but also initial geometric features. In the above studies, only one initial surface hump is considered. However, there are usually many surface humps in a realistic oxide scale. To study the interference of the neighboring surface humps, the periodic humps as shown in Fig. 10 is adopted in the simulation, where Ra_{ini} = 30 nm [22], δ_{ini} = 60 ~ 160 nm and b_{ini} = 30 ~ 90 nm. The oxidation duration is set to be 160 min which is twice of the experimental setting by Li *et al.* [22]. To be more realistic, the variation of the grain diameter of oxide (NiO), d_{g}, with oxidation time is also considered. Based on the experimental results of Huntz *et al.* [25], we linearly increase the grain diameter, d_{g}, from 0.2 μm to 1 μm within 160-min oxidation, expressed in the form of $d_{\mathrm{g}} = \left(0.2 + 0.01 \times t/t_{ref}\right)\mu\mathrm{m}$. Thus, the time dependent diffusion coefficient, $D_{\mathrm{ox}}^{\mathrm{met}}$, can be obtained by substituting the expression of d_{g} in Eq. (26).

Fig. 11

The variation of oxide thickness, h_{ox} (see the definition in Fig. 10), with time is plotted in Fig. 11(a). It is obvious that if the increase of grain diameter is considered, the numerical results agree much better with experimental results [22]. In this case the oxide growth is not

be a conventional parabolic law but sub-parabolic, which has also been report by Huntz *et al.* [25]. The variation of roughness, *Ra* (see the definition in Fig. 10), with time for different initial spacing, δ_{ini}, and half width, b_{ini}, are plotted in Fig. 11(b). It is noted that the roughness increases in the early stage of scale growth and then decreases in the later stage, which has also been observed in the experiments by Li *et al*. [22] and Huntz *et al.* [25]. This is caused by the mutual interference of the growth between the neighboring humps as schematically shown in Fig. 10. In addition, the decrease of roughness slows down with time and the roughness approaches an constant magnitude, Ra^*, after a longtime oxidation.

In Fig. 12(a ~ c), the maximum roughness, Ra_{max}, the critical time to reach it $\underline{t}_c$, and the final roughness, Ra^* (using the roughness magnitude after 160-min oxidation), are plots against initial spacing, δ_{ini}, from 60 ~ 160 nm, and half width, b_{ini}, from 30 ~ 90 nm, respectively. The NiO scale, reaching the maximum roughness, with two different initial geometry ((i) δ_{ini} = 160 nm, b_{ini} = 90 nm and (ii) δ_{ini} = 60 nm, b_{ini} = 30 nm) are also shown in Fig. (a). These three figures illustrate that the roughness of oxide scale can be effectively reduced by changing the geometric features of the initial oxide scale. It is observed that reduction of either δ_{ini} or b_{ini} leads to the decreases of Ra_{max}, t_c, and Ra^*. Comparing with the reduction of b_{ini}, the reduction of δ_{ini}, is more effective in decreasing the roughness of oxide scale. These results suggest a very effective and simple method to suppress the surface roughening of oxide layer and reduce the oxidation-induced failure in industrial applications.

Fig. 12

4. Conclusions

A new phase-field model to study the mechanism of morphology evolution of oxide layer during oxidation is proposed, in which the formula of reaction rate, based on the picture of detailed balance in chemical reaction, is derived and incorporated to describe the migration of phase boundary. The Gibbs free energy density involves the contributions of chemical potential, mechanical deformation, and interfacial anisotropy. And the chemical potentials of reactants and products are the variational derivatives of the total free energy with respect to the corresponding concentration, which are then substituted into the reaction rate formula. The Allen-Cahn type equation, governing the evolution of oxide phase, thus captures the influences of oxidation kinetics, elemental concentration, and mechanical deformation. Associated with the reaction-diffusion equation and the mechanical equilibrium equation, the complete set of phase-field equations were implemented in a computational code based on COMSOL.

The accuracy of the code is first validated by comparing the simulation results with the 1D analytical solutions. For a preliminary understanding of parametric effects, the influence of elemental diffusion and mechanical deformation on the growth of oxide layer is also studied by 1D simulation. It is found that both the reduction of diffusion and the elevation of the eigenstrain can suppress the oxide growth, which is approximately logarithmically dependent on the diffusion coefficient and exponentially scaled with the square of eigenstrain $\left(\varepsilon_{11}^{g}\right)^{2}$. And the map for distinguishing their dominant roles is established based on the curvature of the contour plot.

Based on the 2D simulation, it is found that the surface morphology depends not only on the diffusion rate and eigenstrain but also on the initial morphology of metal surface. When the eigenstrain is larger than the critical value, the oxidation could be suppressed at the flat region of oxide surface while the less constraint convex region grows. Thus, the oxide surface could be extremely rough. In this case, elemental diffusion and the interfacial anisotropy should be the major factors affecting surface roughening. The elevations of the diffusion coefficient and the interfacial anisotropy lead to a taller and sharper surface asperities. By reducing the spacing and the width of surface humps, a significant suppression of surface roughening for oxide scale could be obtained, which might be a very effective and simple method to suppress the surface roughening of oxide layer in industrial application.

Acknowledgments

This work was supported by the Hong Kong Polytechnic University Departmental General Research Funds (G-YBMK), the Early Career Scheme (ECS) of the Hong Kong Research Grants Council (Grant No. 25200515, Account F-PP27). We are grateful for the support.

Conflict of interest

No conflict of interest.

Appendix A

Following the experimental measurement [26], the diffusion of Ni in the grain of NiO and the grain boundary of NiO at one bar pressure are, respectively, in the form of:

$$D_{\mathrm{g}} = 2.2\times10^{-6}\exp\left(-2.56\left(\mathrm{eV}\right)/k_{\mathrm{B}}T\right)\ \left(\mathrm{m}^2/\mathrm{s}\right), \tag{A.1}$$

$$D_{\mathrm{gb}} = 4.3\times10^{-5}\exp\left(-1.78\left(\mathrm{eV}\right)/k_{\mathrm{B}}T\right)\ \left(\mathrm{m}^2/\mathrm{s}\right), \tag{A.2}$$

where eV and k_{B} are, respectively, the electron volt and Boltzmann constant, which are listed in table 1. The width of grain boundary, w_{gb}, and the grain diameter of NiO, d_{g} are $7\times10^{-10}\,\mathrm{m}$ [26] and $2\times10^{-7}\,\mathrm{m}$ [25], respectively. Considering the Eq. (26), the diffusion of Ni in NiO at 973K is $D_{\mathrm{ox}}^{\mathrm{met}} = 1.85\times10^{-16}\,\mathrm{m}^2/\mathrm{s}$.

For the oxidation $a\mathrm{M}+b\mathrm{O} \rightarrow \mathrm{M}_a\mathrm{O}_b$ the Pilling-Bedworth ratio (*PBR*) can be expressed as

$$PBR = \frac{V_{\mathrm{M}_a\mathrm{O}_b}}{aV_{\mathrm{M}}}, \tag{A.3}$$

where $V_{\mathrm{M}_a\mathrm{O}_b}$ and V_{M} are, respectively, the molar volumes of the oxide ($\mathrm{M}_a\mathrm{O}_b$) and the pure metal (M). The mean eigenstrain $\varepsilon_{\mathrm{v}}^{\mathrm{g}}$ due to the transformation from metal to oxide is given as:

$$\varepsilon_{\mathrm{v}}^{\mathrm{g}} = \frac{1}{3}\ln\left(PBR\right), \tag{A.4}$$

In the simulation, the oxidation of pure metal Ni is adopted. The corresponding oxidation can be expressed in the form of Ni+O → NiO. Thus, using V_{NiO} = 11.2 cm^3/mol and V_{Ni} = 6.5 cm^3/mol, the *PBR* = $V_{\mathrm{NiO}}/V_{\mathrm{Ni}}$ is obtained to be 1.72. The mean eigenstrain $\varepsilon_{\mathrm{v}}^{\mathrm{g}}$ is then 0.2. The molar concentration of oxide (NiO) is $c_{\mathrm{NiO}} = 1/V_{\mathrm{NiO}}$ = 89933 mol/m^3. Following Ref. [10], the mole fraction of the diffusible metal (Ni) atom in oxide (NiO) is set to be 1.8% in the present paper. Thus, the reference concentration of oxide (NiO) and free metal (Ni) atom are $c_{\mathrm{ref}}^{\mathrm{ox}}$ = 89933 mol/m^3 and $c_{\mathrm{ref}}^{\mathrm{met}}$ = $0.018c_{\mathrm{ref}}^{\mathrm{ox}}/(1-0.018)$ = 1630 mol/m^3, respectively.

Appendix B

The dimensionless government equation is:

$$\frac{\partial \phi}{\partial \bar{t}} = -\bar{L}_\sigma \left(\bar{W} \frac{\partial g(\phi)}{\partial \phi} - \bar{\sigma}^0 \bar{\zeta}^0 \left(\eta^2 \bar{\nabla}^2 \phi - \frac{\partial}{\partial \bar{x}} \left(\eta \eta' \frac{\partial \phi}{\partial \bar{y}} \right) + \frac{\partial}{\partial \bar{y}} \left(\eta \eta' \frac{\partial \phi}{\partial \bar{x}} \right) \right) \right) - \bar{L}_\kappa \frac{\partial p(\phi)}{\partial \phi} \left(e^{-(1-\rho)\Lambda} - \left(\bar{c}^{\text{met}} \right)^a \left(\bar{c}^{\text{O}} \right)^b e^{\rho \Lambda} \right), \tag{B.1}$$

$$\frac{\partial \bar{c}^{\text{met (or O)}}}{\partial \bar{t}} = \bar{\nabla} \left(\bar{D}^{\text{met (or O)}} \bar{\nabla} \bar{c}^{\text{met}} \right) - a(\text{or } b) \frac{c_{\text{ref}}^{\text{ox}}}{c_{\text{ref}}^{\text{met (or O)}}} \frac{\partial \phi}{\partial \bar{t}} \tag{B.2}$$

and

$$\text{div} \left[\left(p(\phi) \bar{\mathbf{D}}^{\text{e}} \right) \left(\left\{ \frac{1}{2} \left(\frac{\partial \bar{d}_i}{\partial \bar{x}_j} + \frac{\partial \bar{d}_j}{\partial \bar{x}_i} \right) \right\} - p(\phi) \boldsymbol{\varepsilon}^{\text{g}} \right) \right] = 0, \tag{B.3}$$

respectively, where the variables and parameters with the over-head bar are defined as $\bar{L}_\sigma = L_\sigma f_{\text{ref}} t_{\text{ref}}$, $\bar{L}_\kappa = L_\kappa t_{\text{ref}}$, $\bar{\sigma}^0 = \sigma^0/(f_{\text{ref}} l_{\text{ref}})$, $\bar{\zeta}^0 = \zeta^0/l_{\text{ref}}$, $\bar{W} = W/f_{\text{ref}}$, $\bar{D} = D t_{\text{ref}} / l_{\text{ref}}^2$ and $\bar{\mathbf{D}}^{\text{e}} = \mathbf{D}^{\text{e}}/f_{\text{ref}}$.

References

[1] N. P. Padture, Advanced structural ceramics in aerospace propulsion, Nat. Mater. 15(2016) 804–809.

[2] V. Kumar, K. Balasubramanian, Progress update on failure mechanisms of advanced thermal barrier coatings: A review, Prog. Org. Coat., 90 (2016) 54–82.

[3] E. P. Busso, J. Lin, S. Sakurai, and M. Nakayama, A mechanistic study of oxidation-induced degradation in a plasma-sprayed thermal barrier coating system. Part I: Model formulation, Acta Mater. 49 (2001) 1515–1528

[4] L. G. Zhao, N. P. O'Dowd, and E. P. Busso, A coupled kinetic constitutive approach to the study of high temperature crack initiation in single crystal nickel-base superalloys, J. Mech. Phys. Solids. 54 (2006) 288–309.

[5] C. Lin and Y. M. Li, Interface stress evolution considering the combined creep–plastic behavior in thermal barrier coatings, Mater. Des. 89 (2016) 245–254.

[6] C. Lin, Q. Sun, Y. J. Chai, and Y. M. Li, Stress evolution in top coat of thermal barrier coatings by considering strength difference property in tension and compression, Surf. Coat. Technol., 329 (2017) 86–96.

[7] G. Calvarin-Amiri, R. Molins, and A. M. Huntz, Effect of the application of a mechanical Load on the oxide-layer microstructure and on the oxidation mechanism of Ni–20Cr foils, Oxid. Met., 53 (2000) 399–426.

[8] R. Krishnamurthy, D. J. Srolovitz, Stress distributions in growing oxide films, Acta Mater., 51 (2003) 2171–2190.

[9] F. Larche, J.W. Cahn, The interactions of composition and stress in crystalline solids, Acta Metall., 33 (1985) 333–57.

[10] H. Zhou, J. Qu, and M. Cherkaoui, Stress-oxidation interaction in selective oxidation of Cr-Fe alloys, Mech. Mater., 42 (2010) 63–71.

[11] H. Wang, Y. Suo, S. Shen, Reaction-diffusion-stress coupling effect in inelastic oxide scale during oxidation, Oxid. Met. 83 (2015) 507–519.

[12] N. Swaminathan, J. Qu, Y. Sun, An electrochemomechanical theory of defects in ionic solids. I. Theory. Philos. Mag., 87 (2007) 1705–1721.

[13] K. Loeffel and L. Anand, A chemo-thermo-mechanically coupled theory for elastic–visco plastic deformation, diffusion, and volumetric swelling due to a chemical reaction, Int. J. Plasticity 27 (2011) 1409–1431.

[14] K. Loeffel, L. Anand, and Z. M. Gasem, On modeling the oxidation of high–temperature alloys, Acta Mater. 61 (2013) 399–424.

[15] C. Lin and Y. M. Li, A coupled mechanical-chemical model for reflecting the influence of stress on oxidation reactions in thermal barrier coating, J. Appl. Phys., 123 (2018) 215305.

[16] K. Ammar, B. Appolaire, G. Cailletaud, F. Feyel, S. Forest, Finite element formulation of a phase field model based on the concept of generalized stresses, Comp. Mater. Sci., 45 (2009) 800–805.

[17] M. A. Zaeem, H. E. Kadiri, An elastic phase field model for thermal oxidation of metals: Application to zirconia, Comp. Mater. Sci., 89 (2014) 122–129.

[18] Y. Zhao, S. Ai., D.N. Fang, Elasto-plastic phase field modelling of oxidation of zirconium alloys, Int. J. Solids Struct., 134 (2018) 30–42.

[19] Y. Li, X. Fang, B. Xia, X. Feng, In situ, measurement of oxidation evolution at elevated temperature by nanoindentation, Scripta Mater., 103 (2015) 61–64.

[20] X. Fang, Y. Li, C. Zhang, X. Feng, Transition of oxide film configuration and the critical stress inferred by scanning probe microscopy at nanoscale, Chem. Phys. Lett., 660 (2016) 33–36.

[21] X. Fang, Y. Li, D. Wang, S. Lu, and X. Feng, Surface evolution at nanoscale during oxidation: A competing mechanism between local curvature effect and stress effect, J. Appl. Phys., 119 (2016) 1–8.

[22] Y. Li, X. Fang, Z. Qu, S. Lu, H. Li, T. Zhu, Q. Yu and X. Feng, In situ full-field measurement of surface oxidation on ni-based alloy using high temperature scanning probe microscopy, Sci. Rep., 8 (2018) 6684.

[23] A. Atkinson, Transport processes during the growth of oxide films at elevated temperature, Rev. Mod. Phys., 57 (1985) 437–470.

[24] N. Cabrera, N.F. Mott, Theory of the oxidation of metals, Rep. Prog. Phys., 12 (1948) 163–184.

[25] A.M. Huntz, B. Lefevre, F. Cassino, Roughness and oxidation: Application to NiO growth on Ni at 800°C, Mater. Sci. & Eng. A, 290 (2000) 190–197.

[26] A. Atkinson, R.I. Taylor, The Diffusion of 63Ni Along Grain Boundaries in Nickel Oxide, Philos. Mag. A, 43 (1981) 979–998.

[27] S. Mrowec, Z. Grzesik, Oxidation of nickel and transport properties of nickel oxide, J. Phys. Chem. Solids, 65 (2004) 1651–1657.

[28] A. Yamanaka, T. Takaki, Y. Tomita, Phase-Field Simulation of Austenite to Ferrite Transformation and Widmanstätten Ferrite Formation in Fe-C Alloy, Mater. Trans., 47 (2006) 2725–2731.

[29] C. Lin, J. Wan, H.H. Ruan, Phase field modeling of Widmanstätten ferrite formation in steel, J. Alloy Comp., 769 (2018) 620–630.

[30] S.-L. Wang, R.F. Sekerka, A.A. Wheeler, B.T. Murray, S.R. Coriell, R.J. Braun, G.B. McFadden, Thermodynamically-consistent phase-field models for solidification, Physica D, 69 (1993) 189–200.

[31] M. Z. Bazant, Theory of Chemical Kinetics and Charge Transfer based on Nonequilibrium Thermodynamics, Acc. Chem. Res., 46 (2013) 1144–1160.

[32] I. Loginova, J. Ågren, G. Amberg, On the formation of Widmanstätten ferrite in binary Fe-C-phase-field approach, Acta Mater., 52 (2004) 4055–4063.

[33] L. Chen, H. W. Zhang, L. Y. Liang, Z. Liu, Y. Qi, P. Lu, J. Chen, and L.Q. Chen, Modulation of dendritic patterns during electrodeposition: A nonlinear phase-field model, J. Power Sources, 300 (2015) 376–385.

[34] G. Caginalp, Stefan and hele-shaw type models as asymptotic limits of the phase-field equation, Phys. Rev.A, 39 (1989) 5887–96.

[35] R. W. Siegel, Vacancy concentrations in metals, J. Nucl. Mater., 69–70 (1978) 117–146.

[36] A. M. Huntz, G. C. Amiri, H. E. Evans, G. Cailletaud, Comparison of Oxidation-Growth Stresses in NiO Film Measured by Deflection and Calculated Using Creep Analysis or Finite-Element Modeling, Oxid. Met., 57 (2002) 499–521.

[37] A. G. Evans, D. R. Clarke, C. G. Levi, The influence of oxides on the performance of advanced gas turbines, J. Eur. Ceram Soc., 28 (2008) 1405–1419.

[38] COMSOL Multiphysics Users' Guide. Available from: http://www.comsol.com/.

List of figures

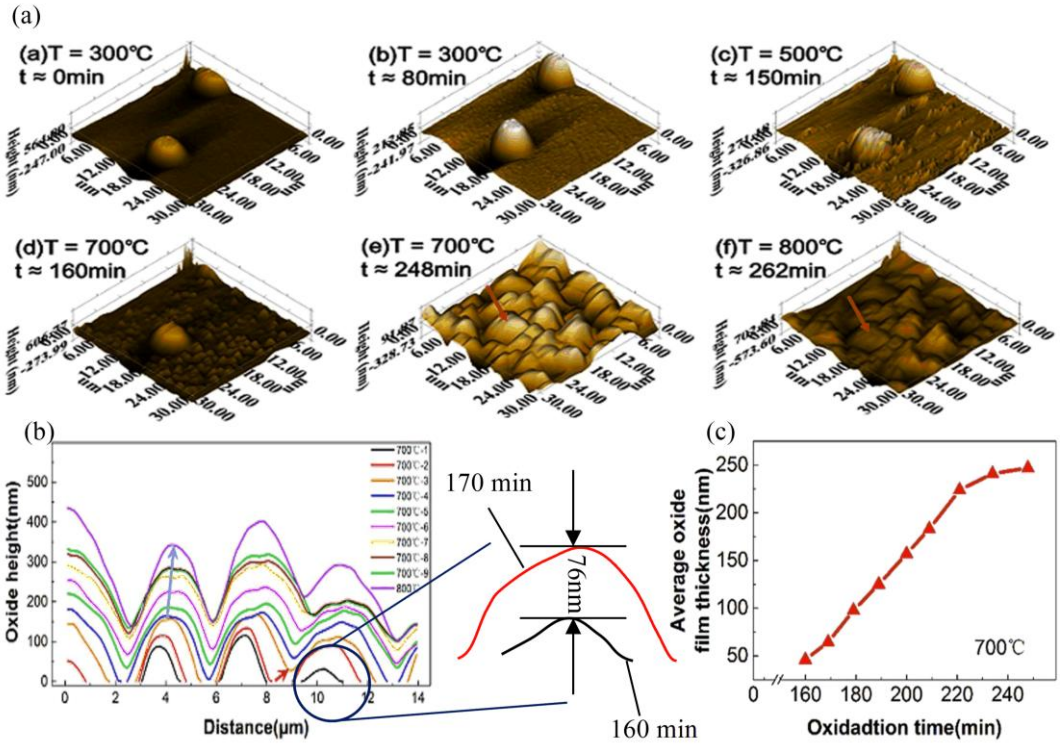

Fig.1 (a) In situ scanning probe microscope images for the surface topography during oxidation (b) roughness change and (c) average oxide film thickness with oxidation time [22].

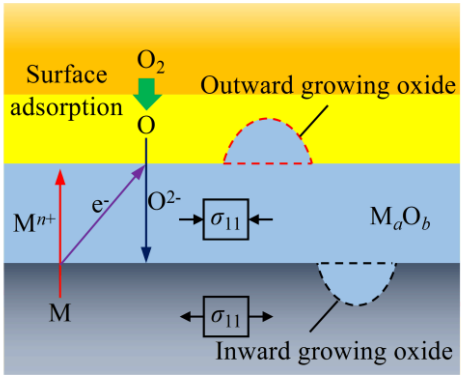

Fig. 2 Diagrammatic sketch of the oxidation of the pure metal. It starts with a surface adsorption step. The gaseous oxygen changes to the atomic oxygen ($O_2 \rightarrow 2O$), which is then adsorbed onto the oxide surface. The adsorbed oxygen atoms are then ionized ($O + 2e^- \rightarrow O^{2-}$), meanwhile the easily oxidized free metal (M) atoms in the substrate are converted to ions at the

M_aO_b/M interface ($M \rightarrow M^{n+} + ne^-$). Consequently, counter diffusion leads to both the oxygen anion O^{2-} and metal cation M^{n+} diffuse into the oxide scale and then the oxidation takes place ($aM^{n+}+bO^{2-} \rightarrow M_aO_b$). Due to the difference in the diffusion rates of reactants, newly formed oxide might grow on the M_aO_b/M interface, called inward growing oxide, or on the M_aO_b/O interface, called outward growing oxide.

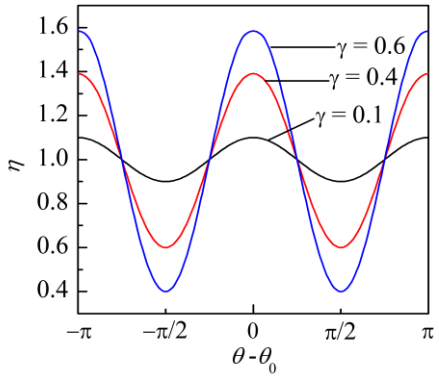

Fig. 3 The plot of anisotropic function, $\eta(\theta)$, against the intersection angle between normal direction of interface and the fastest growth direction, θ - θ_0 , and the strength of interfacial anisotropy, γ.

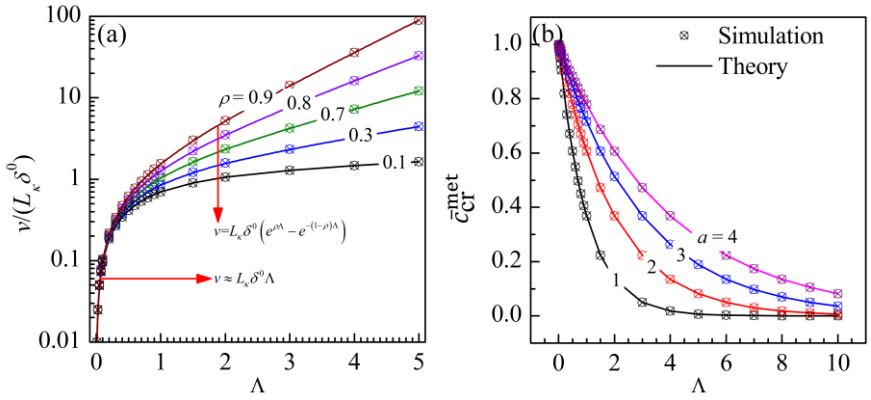

Fig. 4 (a) Variation of the interface migration speed v with the dimensionless reaction driving force Λ and the asymmetry factor ρ, and (b) the relationships between the reaction driving force Λ and the critical elemental concentration $\bar{c}_{cr}^{met}$.

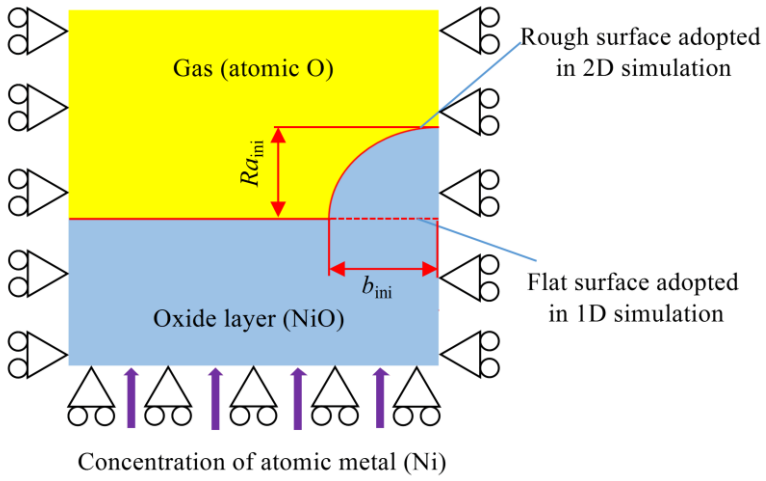

Fig. 5 The schematic of the geometry and boundary conditions in simulation, where the flat and humped interfaces are adopted in 1D and 2D simulations, respectively. b_{ini} is the half width of one hump, and Ra_{ini} is the initial roughness of hump.

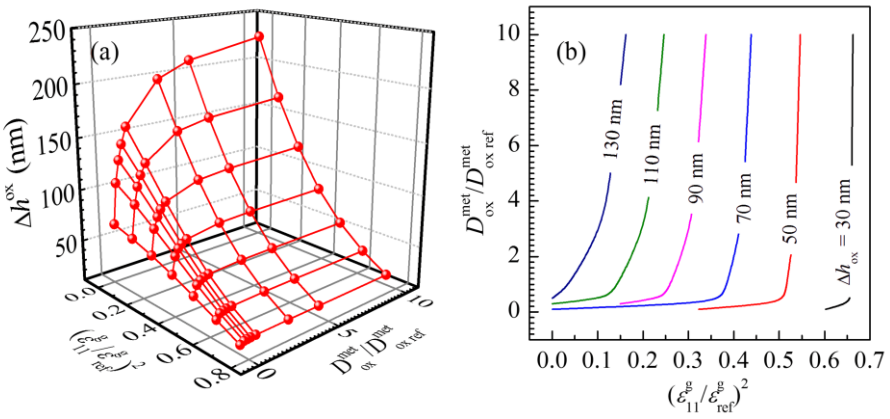

Fig. 6 The variation of thickness of the oxide layer, Δh^{ox}, after 30-min oxidation with the eigenstrain, ε_{11}^{g}, and the diffusion coefficient, D_{ox}^{met}, and (b) Relationship between diffusion coefficient, D_{ox}^{met}, and eigenstrain, ε_{11}^{g}, for constant values, Δh^{ox}.

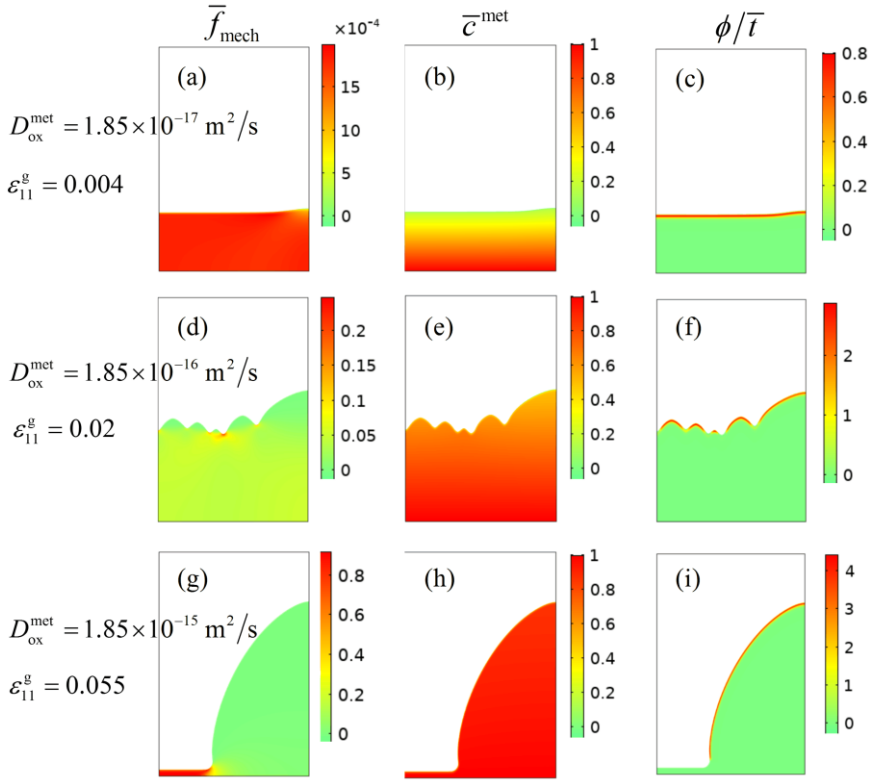

Fig. 7 Counter plots of the elastic energy, the concentration of atomic metal (Ni) and the reaction rate with $D_{\mathrm{ox}}^{\mathrm{met}} = 1.85\times10^{-17} \sim 1.85\times10^{-15}\ \mathrm{m}^2/\mathrm{s}$ and $\varepsilon_{11}^{\mathrm{g}} = 0.004 \sim 0.055$, where $\overline{f}_{\mathrm{mech}} = f_{\mathrm{mech}} / f_{\mathrm{ref}}$ is the dimensionless elastic energy and $\overline{t} = t/t_{\mathrm{ref}}$ is the dimensionless time.

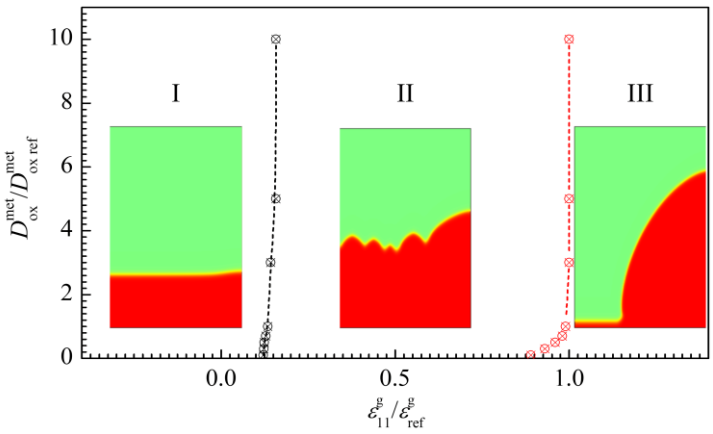

Fig. 8 Phase morphology diagram with the x-axis of eigenstrain and the y-axis of diffusion coefficient, which leads to the three different surface morphologies occurs at three different regions: flat surface in the region I, corrugated surface in the region II and dome-like surface

in the region III.

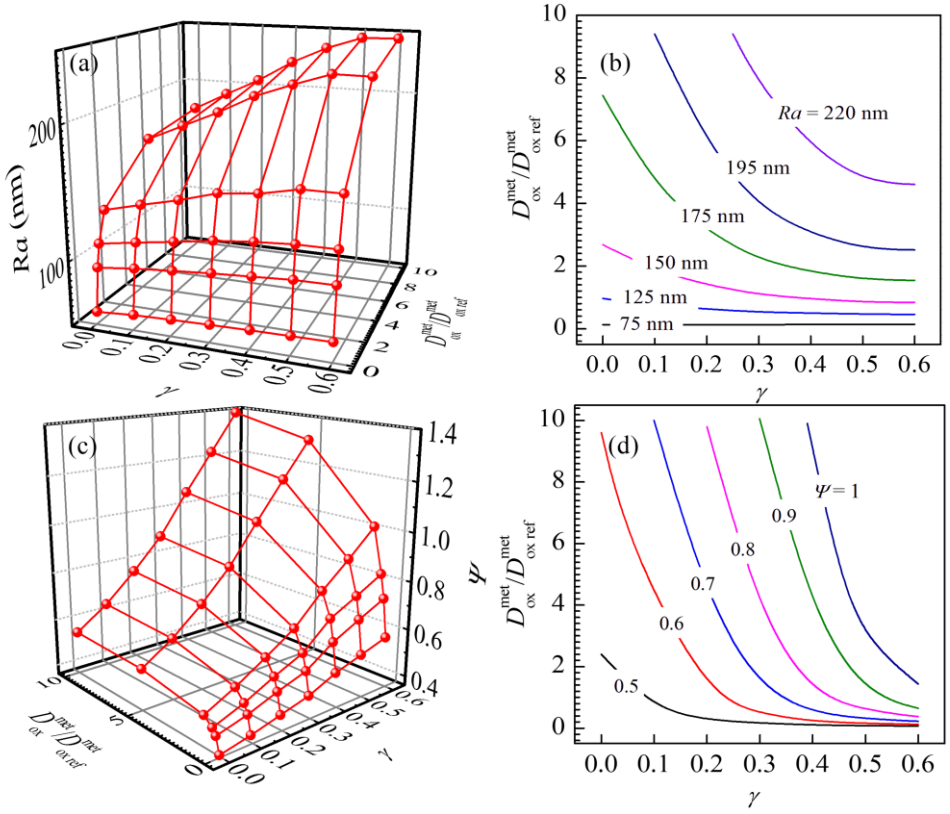

Fig. 9 A initially sinusoidal hump surface of oxide scale adopted in simulation which leads to the numerical results that (a) variation of hump roughness with the diffusion coefficients, D_{ox}^{met}, and the interfacial anisotropy parameter, γ, (b) roughness diagram with the x-axis of strength of interfacial anisotropy, γ, and the y-axis of diffusion coefficient, D_{ox}^{met}, (c) Evolution of aspect ratio of hump, Ψ, with the diffusion coefficients, D_{ox}^{met}, and the strengths of interfacial anisotropy, γ, and (d) aspect ratio, Ψ, diagram with the x-axis of strength of interfacial anisotropy, γ, and the y-axis of diffusion coefficient, D_{ox}^{met}.

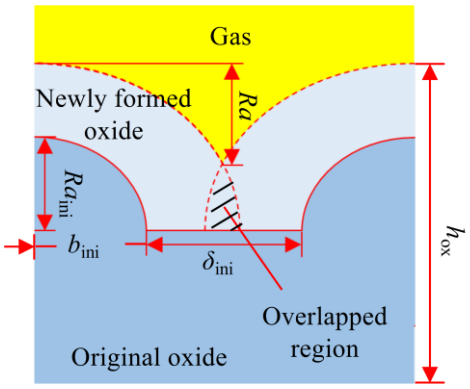

Fig. 10 Diagrammatic sketch of periodic humps, which is adopted to study the interference of the neighboring surface humps. δ_{ini} is the initial spacing between neighboring surface humps, b_{ini} is the half width of one hump, Ra is the roughness of hump and h_{ox} is the oxide thickness.

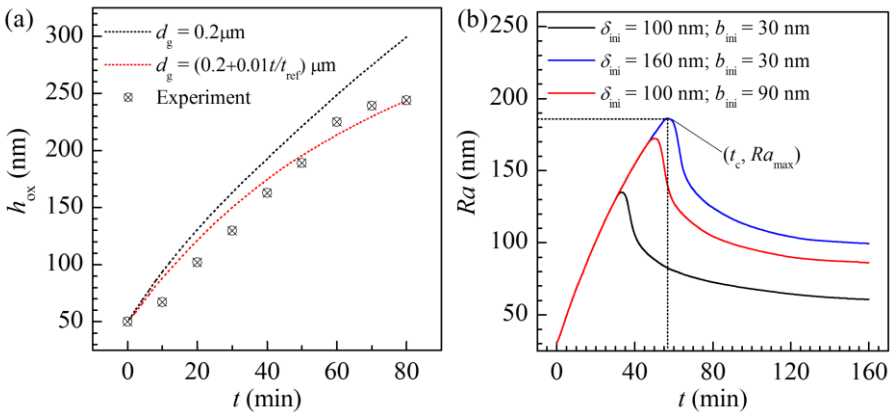

Fig. 11 Plots of (a) Oxide thickness, h_{ox}, with time and (b) roughness, Ra, with time for different initial spacing, δ_{ini}, and half width, b_{ini}, where the experiment results are obtained from Ref. [22].

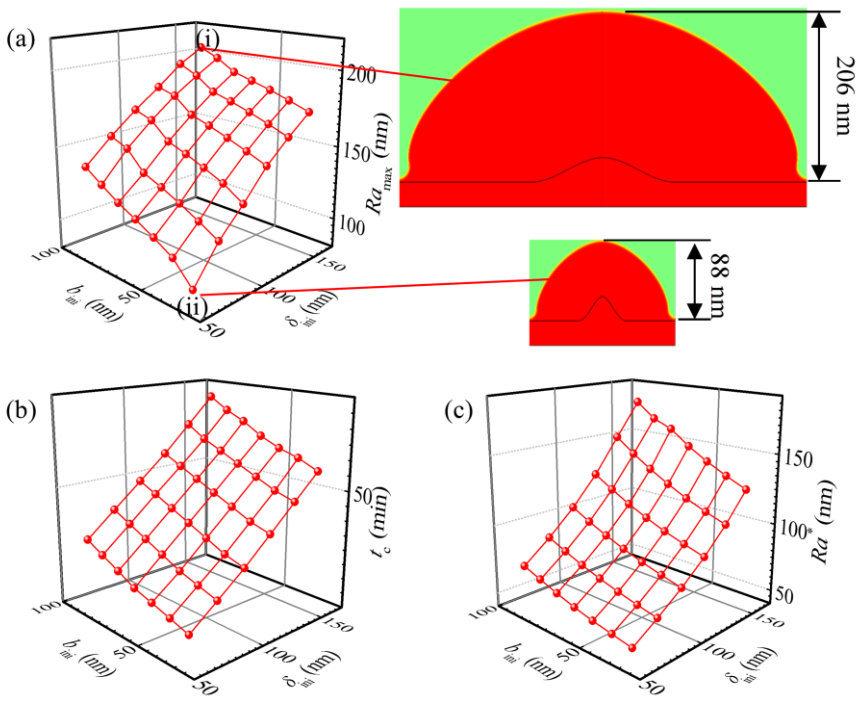

Fig. 12 The initial oxide surface with periodic humps is adopted in simulation, which leads to the numerical results that the variations of (a) maximum roughness, Ra_{max}, (b) critical time, t_c, and (c) final roughness, Ra^* (using the roughness magnitude after 160-min oxidation), against initial spacing, δ_{ini}, from 60 ~ 160 nm, and half width, b_{ini}, from 30 ~ 90 nm.

List of Tables

Table 1.

	Parameter	Value
Interfacial energy density	σ_0 (J/ m^2)	1 [28]
Interface thickness	ζ_0 (nm)	10 [28]
Young's Module for oxide phase	E (GPa)	130
Poisson ratio for oxide phase	ν	0.3
Coefficients to scale the contributions of the interfacial energy	L_σ (m^3/J/min)	10^{-9}
Coefficients to scale the contributions of the oxidation kinetics	L_κ (1/min)	0.075
Excess chemical potential of reactant	μ_1^{ex}	$2RT$
Asymmetry factor	ρ	0.8
Diffusion coefficient of atomic metal (Ni) in the oxide	D_{ox}^{met} (m^2/s)	1.85×10^{-16} (See Appendix A)
Diffusion coefficient of atomic metal (M) in the gas phase[2]	D_{gas}^{met} (m^2/s)	10^{-22}
Strength of interfacial anisotropy	γ	0 ~ 0.6 [28]
The fastest growth direction	θ_0	$\pi/2$ [28]
Reference length	l_{ref} (nm)	10

[2] D_{gas}^{met} is not a realistic physical parameter. We set the small value 10^{-21} m^2/s to avoid singularity in simulation.

Reference time	t_{ref} (min)	2
Reference energy density	f_{ref} (GJ/m^3)	1
Reference concentration of oxide (NiO)	c_{ref}^{ox} (mol/m^3)	89933 (See Appendix A)
Reference concentration of free metal atom (Ni)	c_{ref}^{met} (mol/m^3)	1630 (See Appendix A)
Boltzmann constant	k_B (J/K)	1.38×10^{-23}
electron volt	eV (J)	1.6×10^{-19}
Ideal gas constant	R (J/mol/K)	8.314